Renormalization of quasiparticle band extrema of WSe_2 and $MoTe_2$ homobilayers

Du Li[1], Zhen-Fei Liu[2,*], and Li Yang[1,3,*]

[1]Department of Physics, Washington University in St. Louis, St. Louis, Missouri 63130, USA

[2]Department of Chemistry, Wayne State University, Detroit, Michigan 48202, USA

[3]Institute of Materials Science and Engineering, Washington University in St. Louis, St. Louis, Missouri 63130, USA

ABSTRACT

A fundamental challenge in pursuing topological states in twisted homobilayer transition metal dichalcogenides is the relative energies between the valence band extrema at the topologically trivial Γ and nontrivial K/K' valleys. We employ many-body perturbation theory within the GW approximation to investigate the energy difference of the valence band extrema in homobilayer WSe_2 and $MoTe_2$, the two most promising candidate platforms hosting various quantum phases. In contrast to the results obtained from density functional theory, the GW calculation predicts quasiparticle energies of the K/K' valley above those of the Γ valley for all high-symmetry stackings. We further develop a "fractional folding" technique, allowing for the inclusion of substrate and encapsulating dielectric screening effects in GW simulations. We find that while environmental dielectric screening from h-BN reduces the energy difference between the K/K' and Γ valley extrema, the valence band maximum remains situated at the topologically nontrivial K/K' valley. Finally, many-body effects enhance the depth of the moiré potential, leading to a shift of the "magic angle",

compared to the result from density functional theory. Our study offers quasiparticle energy landscapes to guide the search for twisted homobilayers of topological interest.

I. INTRODUCTION

Layered transition metal dichalcogenides (TMDs) show promise of two-dimensional (2D) semiconducting devices for applications in catalysis, electronics, photovoltaics, and electrochemistry [1-4]. Particularly, the electronic band extremum energy landscapes, e.g., the Γ, K/K' valleys, and Q valleys depicted in Fig. 1(a), can determine abundant fundamental electronic properties. For example, the locations of the valence band maximum (VBM) and the conduction band minimum (CBM) determine whether the electronic band gaps are direct or indirect and are responsible for many important optical and transport features, such as valleytronics and photoluminescence spectroscopy [5-7]. In 2H-phase TMD materials, the K/K' valley, characterized by a non-trivial Berry curvature, plays a crucial role in hosting various quantum phases, e.g., integer and fractional quantum anomalous Hall effects, and doping induced multiferroics [8-14]. Importantly, all these quantum phases prefer the K/K' valley to reside at the VBM to ensure that the doped hole is located at the topologically non-trivial valley.

On the other hand, the energy difference between the valence valleys, denoted as $\Delta^v_{K-\Gamma} = K_v - \Gamma_v$ as illustrated in Fig. 1(a), where K_v and Γ_v represent the band extremum energies at the valence K and Γ valleys, respectively, can be either positive or negative depending on a variety of factors [15-18]. For instance, different stacking configurations, as depicted in Fig. 1(b), can lead to variations in interlayer tunneling and affect $\Delta_{K-\Gamma}$. Particularly for several TMD homobilayers, the valence Γ and K valley energies are so close to each other that $\Delta^v_{K-\Gamma}$ may be tuned experimentally via, e.g., the application of gate voltage [9,12,18]. Meanwhile, many extrinsic factors, e.g., self-doping and substrate effects, can contribute to variations in the measured experimental results [19-22]. Consequently, examining the electronic band-

edge energy landscape to unambiguously identify the VBM is of fundamental importance to understand available measurements and search for new twisted topological TMD homobilayers.

The first-principles density functional theory (DFT) is indispensable to investigate the electronic structures, but it is also known for significantly underestimating band gaps. Particularly, local or semi-local exchange-correlation functionals, e.g., local-density approximation and Perdew–Burke–Ernzerhof (PBE) functional, may yield contradictory results regarding the VBM location in TMD materials [9,12,18,23]. This indicates that more advanced calculations are needed. To date, the more advanced SCAN [9] and the modified Beck-Johnson functional [18], have been applied to address this issue for specific stacking configurations. Furthermore, current theoretical studies predominantly focus on the suspended topological moiré TMD bilayers. The impact of environments, such as substrate and encapsulation (illustrated in Figs. 1(c) and (d)), on the valence band extrema and moiré potential remains unexplored.

In this work, given the dramatically enhanced many-body effects in 2D structures [24-26], we employ the first-principles many-body perturbation theory (MBPT) within the GW approximation [27] to study the renormalization of quasiparticle bands extrema in different stackings of homobilayer WSe_2 and $MoTe_2$, the two most promising candidate platforms hosting various quantum phases. We find that the GW calculation predicts that the extremum at the valence K valley is energetically much higher than that at the Γ valley, compared to DFT results, and the quasiparticle VBM is located at the K valley for all stackings. To reduce the computational cost for TMDs supported by a substrate or encapsulated by another material, we have developed a "fractional folding" technique to include the dielectric screening effect of hexagonal boron nitride (h-BN) as a substrate and encapsulation material, which is the most common one used in experiments. Our results indicate that external dielectric screening effects reduce $\Delta^{v}_{K-\Gamma}$, but the VBM remains located

at the *K* valley. To this end, we demonstrate the renormalizations of the moiré potentials and moiré mini bands from many-body interactions. The depth of moiré potential is increased by 36-52%, and many-body effects alter the value of the "magic angle" compared to DFT results.

The remainder of this article is organized as follows: In Sec. II, we present the computational details of DFT and *GW* calculations. In Sec. III, the results of suspended TMD homobilayers are presented and discussed. In Sec. IV, we develop the "fractional folding" technique and discuss the *h*-BN substrate/encapsulation screening effects on the relative energies of valence band extrema, $\Delta^{v}_{K-\Gamma}$. In Sec. V, we compare the moiré potentials obtained by various theoretical approaches. The influences from many-body interactions on the bandwidth of the first moiré mini band are discussed. Finally, the conclusions are summarized in Sec. VI.

II. COMPUTATIONAL DETAILS

The DFT calculation is performed using the PBE exchange–correlation functional with SOC including semi-core electrons [28,29], as implemented in the Quantum ESPRESSO package [30]. A wavefunction cutoff of 60 Ry, a charge density cutoff of 240 Ry, and a 12 × 12 × 1 k-grid are adopted. For 2D structures, the van der Waals (vdW) interaction is included via the semiempirical Grimme-D3 scheme [31]. A vacuum of 18 Å between adjacent layers is used to avoid spurious interactions between periodic images along the out-of-plane direction of 2D structures.

The single-shot G_0W_0 calculations are performed using the BerkeleyGW package [32]. As the first step, we compute the static non-interacting Kohn-Sham (KS) polarizability, χ^0, using Eq. (1):

$$\chi^0_{\boldsymbol{GG'}}(\boldsymbol{q},\omega=0)=\sum_{v,c,\boldsymbol{k}}\frac{\left\langle v,\boldsymbol{k}+\boldsymbol{q}\middle|e^{i(\boldsymbol{q}+\boldsymbol{G})\cdot\boldsymbol{r}}\middle|c,\boldsymbol{k}\right\rangle\left\langle c,\boldsymbol{k}\middle|e^{-i(\boldsymbol{q}+\boldsymbol{G'})\cdot\boldsymbol{r'}}\middle|v,\boldsymbol{k}+\boldsymbol{q}\right\rangle}{E_{v,\boldsymbol{k}+\boldsymbol{q}}-E_{c,\boldsymbol{k}}}, \quad (1)$$

where $\boldsymbol{q}$ and $\boldsymbol{k}$ are vectors in the first Brillouin zone, $\boldsymbol{G}$ is a reciprocal-space lattice vector. v refers to occupied (valence) states and c refers to unoccupied (conduction) states. $|v, \boldsymbol{k}+\boldsymbol{q}\rangle$, $|c, \boldsymbol{k}\rangle$, $E_{v,\boldsymbol{k}+\boldsymbol{q}}$, and $E_{c,\boldsymbol{k}}$ are the KS eigenvectors and eigenvalues, respectively. Then the static dielectric matrix ϵ is computed from the KS χ^0 using Eq. (2):

$$\epsilon(\boldsymbol{q}; \boldsymbol{G}, \boldsymbol{G}') = \delta_{\boldsymbol{G}\boldsymbol{G}'} - v(\boldsymbol{q}+\boldsymbol{G})\chi^0(\boldsymbol{q}; \boldsymbol{G}, \boldsymbol{G}'), \tag{2}$$

where $v(\boldsymbol{q}+\boldsymbol{G})$ is the bare Coulomb interaction, i.e., $v(\boldsymbol{q}+\boldsymbol{G}) = 4\pi/|\boldsymbol{q}+\boldsymbol{G}|^2$. Notably, in practical applications, the formulation of the bare Coulomb interaction can be modified based on the specific truncation methods selected for the system [33]. Then, the static screened Coulomb interaction is calculated using Eq. (3):

$$W(\boldsymbol{q}; \boldsymbol{G}, \boldsymbol{G}') = \epsilon^{-1}(\boldsymbol{q}; \boldsymbol{G}, \boldsymbol{G}')\, v(\boldsymbol{q}+\boldsymbol{G}')\,, \tag{3}$$

The Hybertsen–Louie generalized plasmon-pole model is used to treat the frequency dependence of the dielectric function [27]. The static remainder approximation [34] is used in the evaluation of the self-energy for faster convergence. SOC is considered as a perturbation to the self-energy correction [23,35]. The slab Coulomb truncation [33] is adopted to remove the spurious long-range Coulomb interactions along the non-periodic direction. An $18 \times 18 \times 1$ and a $15 \times 15 \times 1$ (as discussed in Supplementary Material Sec. I) q-grid is adopted to calculate the polarizability and quasiparticle energies for bilayer WSe_2 and $MoTe_2$, respectively. Given the slow convergence behavior of quasiparticle band extrema in TMD materials as discussed in Supplementary Material Sec. I, a high screened Coulomb energy cutoff 35 Ry is used.

III. SUSPENDED TMD HOMOBILAYERS

We consider the five high-symmetry stacking configurations of the suspended TMD homobilayers, as depicted in Fig. 1(b). As two typical examples, Fig. 2 presents the electronic

structure of bilayer WSe_2 and $MoTe_2$ in their natural bulk $H_X^M(AA')$ stacking. Our calculated in-plane lattice constants for bilayer WSe_2 and $MoTe_2$ are 3.30 Å and 3.53 Å, respectively, which agree well with experimental values [6,23,36,37]. In bilayer WSe_2, DFT results show that the valley energy difference is $\Delta^v_{K-\Gamma}$ = -53 meV, and the VBM is located at the Γ valley as demonstrated in Figs. 2(a) and 2(c). The K-to-K direct gap is 1.22 eV, and the Γ-to-K indirect gap is 1.17 eV. To obtain a more accurate description of the bandgap and extremum energies, we perform the GW calculation, as illustrated in Figs. 2(b). Many-body effects substantially increase bandgaps compared to the DFT results. The quasiparticle K-to-K direct and Γ-to-K indirect gaps are increased to 2.16 and 2.25 eV, respectively. These values agree well with previous GW results [38-40].

Importantly, electronic self-energy corrections are different for the K and Γ valleys. A more substantial GW correction at the Γ point moves the Γ valley lower than the K valley. Consequently, the GW calculation reverses the sign of the DFT valley-energy difference, yielding $\Delta^v_{K-\Gamma}$= 88 meV and elevating the K valley to be the VBM, as illustrated in Fig. 2(c). This difference in the self-energy corrections can be explained by the different electron localization of the states at these two valleys. Our calculation shows that the quasiparticle effective mass is 0.45 m_0 at the valence K valley and 1.56 m_0 at the Γ valley, respectively, where m_0 represents the electron rest mass. The larger effective mass indicates that the in-plane wavefunction is more spatially localized at the Γ valley, which leads to an enhanced contribution of the screened exchange interaction (Σ_{SX}) to the self-energy correction at the valence Γ valley (as discussed in Supplementary Material Sec. II). Consequently, there is a more substantial GW correction at the valence Γ valley, moving its energy below that of the K valley.

For the conduction valleys, DFT calculations indicate the Q valley is the CBM in bilayer WSe_2. However, the exact location of the CBM remains ambiguous, since the K and Q valleys are almost degenerate, with an energy difference of only 8 meV as depicted in Fig. 2(a).

Notably, many-body effects are expected to induce a larger correction to the conduction K valley, which will elevate the K valley above the Q valley. The reason is similar to the previous discussion of the VBM. As shown in Fig. 2(b), our GW calculation confirms this speculation and increases the K- Q valley energy difference Δ^{c}_{K-Q} to 260 meV, signifying that the Q valley is the CBM.

Aside from the natural bulk stacking, the valley energy differences obtained from DFT and GW calculations for all stacking configurations are summarized in Table I. For the valence valleys in WSe_2, similar to the H^{M}_{X} stacking, many-body effects convert $\Delta^{v}_{K-\Gamma}$ from negative values (-18 meV and -24 meV) to positive values (102 meV and 112 meV) for the H^{M}_{M} and R^{M}_{X} stackings, respectively. For the conduction valleys, a similar change in the sign of Δ^{c}_{K-Q} is observed for the H^{M}_{M} and H^{X}_{X} stackings, as we show in Table I.

Interestingly, DFT and GW yield the same signs for $\Delta^{v}_{K-\Gamma}$ in the H^{X}_{X} and R^{M}_{M} stacking configurations for bilayer WSe_2. This can be understood from the interlayer interaction and screening effects. As listed in Table I, the interlayer distance is larger by approximately 0.6 Å in the H^{X}_{X} and R^{M}_{M} stackings compared to other stacking configurations. Notably, the DFT calculated interlayer distances may depend on the exchange-correlation functionals and van-der-Waals correction scheme [18,41]. But the trend that the H^{X}_{X} and R^{M}_{M} stackings have a larger interlayer distance remains valid. The valence Γ valley exhibits a more pronounced interlayer hybridization effect than that in the K valley, making the Γ valley more sensitive to the interlayer spacing distance. Such larger interlayer distances in the H^{X}_{X} and R^{M}_{M} stackings reduce the interlayer hybridization, lowering the energy of the Γ valley. Consequently, at the DFT level, $\Delta^{v}_{K-\Gamma}$ equals 155 and 191 meV for the H^{X}_{X} and R^{M}_{M} stackings, respectively. Moreover, the larger interlayer distance weakens the screening effects and many-electron interactions. Therefore, the GW corrections for $\Delta^{v}_{K-\Gamma}$ in H^{X}_{X} and R^{M}_{M} stackings are 50-60 meV smaller than those in the H^{M}_{X}, H^{M}_{M}, and R^{M}_{X} stackings.

Figures 2(d)-2(f) present DFT and quasiparticle band structures for the H_X^M stacking of bilayer $MoTe_2$, respectively. In contrast to bilayer WSe_2, both DFT and *GW* calculations designate the *K* valley as the VBM across all stackings. As shown in Table I, *GW* calculations augment $\Delta_{K-\Gamma}^{v}$ by approximately 200 meV for H_X^M, H_M^M, and R_X^M stackings and around 100 meV for H_X^X and R_M^M stackings, respectively, compared to DFT results. This is again due to the large self-energy correction at the valence *Γ* valley, similar to bilayer WSe_2. This result suggests that bilayer $MoTe_2$ can be more heavily doped for observing various quantum phases based on the doped hole at the *K* valley. For the conduction bands, both DFT and *GW* calculations predict a positive sign for Δ_{K-Q}^{c} across all stacking orders, but the *GW* values are larger by about 150 meV. Tables SII and SIII in the Supplementary Material list detailed information on the electronic band extremum energies obtained by DFT and *GW* calculations of suspended homobilayer WSe_2 and $MoTe_2$.

IV. ENVIRONMENTAL DIELECTRIC SCREENING EFFECTS

The above calculations are for suspended bilayers. However, in realistic experimental settings, the environmental dielectric screening effects also play a significant role in modulating the quasiparticle electronic structure [24,42-47]. In this section, we investigate how the external substrate and encapsulation influence the quasiparticle band extrema at the valence *Γ* and *K* valleys in bilayer WSe_2 and $MoTe_2$. We consider *h*-BN as the substrate or encapsulation material in this work, which is widely used in experiments [8,14,20]. In our calculations, we include two layers of *h*-BN as the substrate/encapsulation material. The approach we develop can be readily extended to other substrate or encapsulation materials. We employ the substrate screening approximation [Eq. (4)] to include the screening effects of *h*-BN in the KS polarizability. As TMD bilayer and *h*-BN exhibit neglectable hybridization, the total KS polarizability χ^0 can be divided into two terms:

$$\chi^0 \approx \chi^0_{TMD} + \chi^0_{hBN}, \tag{4}$$

where χ^0_{TMD} is the KS polarizability of the bilayer TMD and χ^0_{hBN} is the contribution from the *h*-BN substrate or encapsulation. To address the lattice mismatch within 1% between the TMD bilayer (~3.30 Å for WSe_2) and *h*-BN (~2.50 Å), traditional *GW* calculations often construct an interface consisting of a 3 × 3 TMD supercell and a 4 × 4 *h*-BN supercell, as depicted in Fig. 3(a) and 3(b). However, the supercell *GW* calculations are computationally expensive [32,48]. Additionally, an accurate determination of the peculiar energy extrema in TMD materials requires a high energy cutoff of 35 Ry for the screened Coulomb energy, which is substantially larger than what is required to converge the direct band gap (~10 Ry). This high energy cutoff poses a further challenge for supercell *GW* self-energy calculations, even after Eq. (4) is used to address the computational cost of KS polarizability. As an example, at an energy cutoff of 35 Ry, 6023 *G*-vectors are necessary in a primitive cell calculation and 52516 *G*-vectors are necessary in a supercell calculation, respectively, compared to 1233 *G*-vectors in a primitive cell TMD when the energy cutoff is 10 Ry.

We propose a "fractional folding" technique to circumvent a supercell *GW* calculation, as depicted in the schematic flowchart of Fig. 3(c). This idea is an extension of the folding technique that was originally developed in the context of weakly coupled interface systems [42-45]. The workflow of fractional folding can be described as the following procedures (using bilayer WSe_2 and *h*-BN interface as an example):

$$\chi^0_{\mathrm{hBN}(1\times1)}(\boldsymbol{q_1}+\boldsymbol{G_1},\boldsymbol{q_1}+\boldsymbol{G'_1}) \xrightarrow{\text{folding}} \chi^0_{\mathrm{hBN}(4\times4)}(\boldsymbol{q}+\boldsymbol{G},\boldsymbol{q}+\boldsymbol{G'}) \tag{5}$$

$$\xrightarrow{\text{unfolding}} \chi^0_{\mathrm{hBN}(4/3\times4/3)}(\boldsymbol{q_2}+\boldsymbol{G_2},\boldsymbol{q_2}+\boldsymbol{G'_2}).$$

We list the five steps of the fractional folding below. (I) We calculate the KS χ^0 of the *h*-BN unit cell $\chi^0_{\mathrm{hBN}(1\times1)}(\boldsymbol{q_1}+\boldsymbol{G_1},\boldsymbol{q_1}+\boldsymbol{G'_1})$, where $\boldsymbol{G_1}$, $\boldsymbol{G'_1}$ are the reciprocal lattice vectors and $\boldsymbol{q_1}$ is a vector in the first Brillouin zone of the *h*-BN unit cell. A 24 × 24 × 1 $\boldsymbol{q}$-mesh is used for this calculation. (II) Then, we fold the *h*-BN unit-cell KS χ^0 to a 4 × 4 × 1 supercell $\chi^0_{\mathrm{hBN}(4\times4)}(\boldsymbol{q}+\boldsymbol{G},\boldsymbol{q}+\boldsymbol{G'})$ on a $\boldsymbol{q}$-mesh of 6 × 6 × 1, where $\boldsymbol{G}$, $\boldsymbol{G'}$ are reciprocal lattice vectors and $\boldsymbol{q}$ is a

vector in the first Brillouin zone of the supercell. Note that this 4 × 4 × 1 *h*-BN supercell is commensurate with a 3 × 3 × 1 TMD supercell, i.e., $\chi^0_{\mathrm{hBN}(4\times4)}$ and $\chi^0_{\mathrm{TMD}(3\times3)}$ share the same dimension. The folding is realized by matching the $\boldsymbol{q}$ and $\boldsymbol{G}$ vectors between the unit cell and the supercell, i.e., $\boldsymbol{q}+\boldsymbol{G}=\boldsymbol{q_1}+\boldsymbol{G_1}$ and $\boldsymbol{q}+\boldsymbol{G'}=\boldsymbol{q_1}+\boldsymbol{G'_1}$, because $\chi^0_{\mathrm{hBN}(1\times1)}$ and $\chi^0_{\mathrm{hBN}(4\times4)}$ contain the same physical information. This is discussed in detail in Ref. [42]. (III) After we obtain the supercell *h*-BN KS χ^0, we unfold it to the TMD unit cell on a $\boldsymbol{q}$-mesh of 18 × 18 × 1, and call this quantity $\chi^0_{\mathrm{hBN}(4/3\times4/3)}(\boldsymbol{q_2}+\boldsymbol{G_2},\boldsymbol{q_2}+\boldsymbol{G'_2})$, where $\boldsymbol{G_2}$, $\boldsymbol{G'_2}$ are the reciprocal lattice vectors and $\boldsymbol{q_2}$ is a vector in the first Brillouin zone of the TMD unit cell. The unfolding is realized by $\boldsymbol{q}$- and $\boldsymbol{G}$-vector matching similar to the folding step. We emphasize that the dimension of $\chi^0_{\mathrm{hBN}(4/3\times4/3)}(\boldsymbol{q_2}+\boldsymbol{G_2},\boldsymbol{q_2}+\boldsymbol{G'_2})$ is commensurate with that of $\chi^0_{\mathrm{TMD}(1\times1)}$ due to lattice matching, which makes the $\boldsymbol{q}$- and $\boldsymbol{G}$-vector matching feasible in the unfolding step. This is why we term this process "fractional folding", and the resulting $\chi^0_{\mathrm{hBN}(4/3\times4/3)}$ is equivalent to the KS χ^0 of a fictitious 4/3 × 4/3 × 1 *h*-BN "effective fractional cell" (one that shares the same lattice constants as a TMD unit cell). (IV) We add the resulting *h*-BN $\chi^0_{\mathrm{hBN}(4/3\times4/3)}$ to the directly calculated TMD unit cell $\chi^0_{\mathrm{TMD}(1\times1)}$ based on Eq. (4). The resulting KS χ^0 and the related ϵ defined in Eq. (2) define the dielectric environment that TMD "feels" when it is interfaced with *h*-BN. (V) Finally, we perform embedding *GW* self-energy calculations in the TMD unit cell using the ϵ calculated in the last step, similar to those in the context of weakly coupled interfaces [49]. Here, the Green's function is computed for the TMD unit cell only, while the screened Coulomb interaction calculated using Eq. (3) takes into account the effect of *h*-BN.

This method avoids direct *GW* calculation of the supercell, in both steps of the KS polarizability and the self-energy. As a result, the overall computational cost is comparable to *GW* calculations of a TMD unit cell. To validate the accuracy of our fractional folding approach, we used an interface of monolayer WSe_2 and monolayer *h*-BN as a benchmark test case (as discussed in the Supplementary Material Sec. IV). We have verified that for the *K*-

to-K direct gap, the fractional folding technique yields an error of ~10 meV, compared to the direct calculations of the interface, indicating a good accuracy. For the h-BN encapsulation, χ^0_{hBN} includes contributions from both top and bottom h-BN layers with the "fractional folding" process similar to the substrate case.

The external screening effects from h-BN bilayers substrate/encapsulation on the Γ and K valleys of bilayer WSe_2 and $MoTe_2$ are summarized in Fig. 4. We note that we focus on the valence bands in this work because their properties are more relevant to various quantum phases than those of the conduction bands. Using the bilayer WSe_2 $H_X^M(AA')$ stacking as a representative example, we can see that the external screening effects decrease the bandgaps. For instance, when placed on the h-BN substrate, the K-to-K direct gap of bilayer WSe_2 is 2.10 eV and the Γ-to-K indirect gap is 2.16 eV, respectively, a reduction of 60 meV for the K-to-K direct gap and 93 meV for the Γ-to-K indirect gap from the suspended case, respectively. When the h-BN substrate effect is included, $\Delta^v_{K-\Gamma}$ becomes 55 meV, a reduction of 33 meV from the freestanding scenario. When a h-BN encapsulation environment is considered, $\Delta^v_{K-\Gamma}$ is further reduced to 14 meV. Other stacking configurations demonstrate the similar trend, as depicted in Fig. 4(a). Environmental screening effects reduce $\Delta^v_{K-\Gamma}$ and elevate the energy extremum at the Γ valley. Nevertheless, the K valley consistently remains as the VBM for all stacking configurations.

Similarly, for bilayer $MoTe_2$ as illustrated in Fig. 4(b), the substrate and encapsulation screening environment can reduce the value of $\Delta^v_{K-\Gamma}$. However, it does not reverse the sign of $\Delta^v_{K-\Gamma}$, and the K valley remains the global VBM. This conclusion supports the idea of realizing various quantum phases based on the valence K valley of both bilayer WSe_2 and $MoTe_2$. For more detailed information on the electronic band extremum energies obtained by different theoretical strategies, please refer to Table SII-SV in the Supplementary Materials.

V. MOIRÉ POTENTIAL AND MINIBANDS

To investigate the many-body effects and external screening influences on the moiré potential and moiré mini bands, we employ the following Eq. (6) to describe the dependence of the homobilayers valence extrema energy on the relative displacement $\boldsymbol{r_0}$ between the aligned layers [9,12,50], where the C_3 symmetry in the homobilayer leads to the two-parameter (m_1, ϕ) formalism of the potential:

$$M(\boldsymbol{r_0}) = m_0 + 2m_1 \sum_{j=1,3,5} \cos(\boldsymbol{G}_j \cdot \boldsymbol{r_0} + \phi), \quad (6)$$

where m_0 is a constant and referenced with respect to the vacuum level. $\boldsymbol{r_0}$ is the displacement between the aligned layers. The summation runs over the three nearest neighbor reciprocal lattices in two dimensions, and $\boldsymbol{G}_j = 4\pi/(\sqrt{3}a_M)(cos2\pi\frac{j-1}{3}, sin2\pi\frac{j-1}{3})$, where $j = 1,3,5$. a_M is the monolayer lattice constant. m_1 characterizes the amplitude of the potentials and is decided by the relative energy position of the investigated valley with respect to different stacking configurations (band extremum energies obtained by different methods referenced to the vacuum level are shown in the Supplementary Materials Tables SII-V). ϕ characterizes the shape of the potentials to keep the C_3 symmetry. In practice, to describe the moiré potential $M(\boldsymbol{r})$ experienced by electrons from the valence band extrema due to the moiré superlattice with a twist angle θ, $\boldsymbol{r_0}$ is replaced by $\theta\hat{z} \times \boldsymbol{r}$ in Eq. (6), approximating the local displacement between the two layers. Fig. 5 presents the moiré potentials of *R* stacking bilayer WSe_2 and $MoTe_2$, obtained using different theoretical approaches. For bilayer WSe_2 as depicted in Figs. 5(a-d), DFT-calculated moiré potentials from the *Γ* and *K* valleys overlap with each other, with the *Γ* moiré potential being the VBM. *GW* calculations demonstrate that the *Γ* and *K* moiré potentials have a Δ = 77 meV separation. Here, Δ is defined as the energy difference between the global minimum of the *K* moiré potential and the global maximum of the *Γ* moiré potential, which differs from $\Delta^v_{K-\Gamma}$ for a single stacking configuration discussed in the previous sections. Environmental screening effects can reduce the energy separation between the *Γ* and *K* moiré potentials. When a *h*-BN bilayer substrate is included, Δ = 50 meV, while Δ decreases to 17 meV when a *h*-BN bilayer encapsulation

environment is considered. The results for $MoTe_2$, shown in Figs. 5(e-h), are similar to those in WSe_2. Many-body effects can augment Δ while external screening effects reduce it. Overall, in *GW* results, the *Γ* and *K* moiré potentials always have a positive energy separation Δ, and globally *K* moiré potential remains the VBM. Furthermore, the energy difference, Δ, in $MoTe_2$ is consistently 150-170 meV higher than in WSe_2 across all scenarios, whether it is freestanding, on a substrate, or encapsulated. This significant difference indicates that bilayer $MoTe_2$ has a greater potential for heavy doping to support a variety of quantum phases.

Since the *K* valley has a topologically non-trivial Berry curvature, the moiré potential originating from the *K* valley is primarily of concern in this section, as depicted in Figs. 6(a) and 6(b). For WSe_2, the DFT-calculated moiré potential depth is ~25 meV. Including many-body effects, the moiré potential depth is renormalized and increases by 36% to 34 meV. For $MoTe_2$, the DFT-calculated moiré potential depth is 23 meV, and the *GW* moiré potential depth is 35 meV, a 52% increase owing to the many-body effects. Interestingly, the dielectric screening from an external *h*-BN substrate or encapsulation can significantly impact the relative valence energy difference between the *Γ* and *K* valleys, as illustrated in Fig. 5. However, we find that they only have minor modulations (2-3 meV) on the moiré potential depth.

The renormalized moiré potential depth by the many-body effects can alter the behaviors of moiré mini bands. The continuum model Hamiltonian for the *K* valley moiré mini bands is given by Eq. (7) (the fitting parameters are listed in Supplementary Materials Sec. V):

$$\mathcal{H} = \begin{pmatrix} -\frac{\hbar^2(\boldsymbol{k}-\boldsymbol{\kappa}_+)^2}{2m^*} + M_1(\boldsymbol{r}) & T(\boldsymbol{r}) \\ T^\dagger(\boldsymbol{r}) & -\frac{\hbar^2(\boldsymbol{k}-\boldsymbol{\kappa}_-)^2}{2m^*} + M_2(\boldsymbol{r}) \end{pmatrix}. \tag{7}$$

where the Hamiltonian consists of a two-by-two matrix accounting for the two layers. The off-diagonal elements represent the interlayer coupling, where $T(\boldsymbol{r}) = w(1 + e^{-i\boldsymbol{G}_2\cdot\boldsymbol{r}} + e^{-i\boldsymbol{G}_3\cdot\boldsymbol{r}})$. w

is the tunneling strength parameter decided by the band splitting at the valence K valley, which is induced by the ferroelectricity of the R stacking. The diagonal elements comprise the kinetic term and the moiré potential terms $M_1(\boldsymbol{r})$ and $M_2(\boldsymbol{r})$ for the bottom and top layers, respectively. $M_{1,2}(\boldsymbol{r})$ are determined by Eq. (6), where 1,2 indicates different layers and have opposite signs of ϕ. $\boldsymbol{\kappa}_{\pm}$ points of the moiré Brillouin zone are formed from the K points of the twisted monolayer Brillouin zones. Notably, in practice, the twisted angle θ enters $M_{1,2}(\boldsymbol{r})$ and $T(\boldsymbol{r})$ by replacing $\boldsymbol{r}$ by $\theta\hat{z}\times\boldsymbol{r}$. And the moiré period is a_M/θ. The continuum model Hamiltonian is solved in the moiré mini Brillouin zone using the reciprocal lattice constant b, where $b = 8\pi\sin(\theta/2)/\sqrt{3}a_M$.

We employ Eq. (7) to study the moiré mini bands using moiré potentials obtained from DFT and GW calculations, respectively. The bandwidth of the first moiré band, denoted as W, is plotted as a function of the twisted angle in Figs. 6(c) and 6(d). The first moiré band can achieve almost perfect flatness near a "magic angle" θ_m and is a crucial feature for studying fractional quantum anomalous Hall phases [9]. For WSe_2, the DFT moiré mini band has a magic angle at θ_m^{DFT} = 1.41° that agrees well with previous DFT calculation results [9]. Including many-body effects, the GW calculation yields a larger magic angle at θ_m^{GW} = 1.52°. Similarly, for $MoTe_2$, the renormalized moiré potential increases the magic angle from θ_m^{DFT} = 1.65° to θ_m^{GW} = 1.87°. To conclude, many-body effects can augment moiré potential depth by 36-52%, alter the moiré mini bands, and shift the magic angle to a larger value.

It is important to note that this study focuses on highlighting a single factor: the significance of many-electron interactions in influencing the valence band extrema and the resulting moiré potentials. Previous research [51,52] has demonstrated that structural reconstructions and piezoelectric effects may also play a crucial role in shaping the moiré potential and subsequent moiré mini bands. A comprehensive analysis incorporating all these factors would necessitate direct moiré-supercell calculations. Such an extensive investigation falls

outside the scope of our current work but presents a promising avenue for future research endeavors.

VI. CONCLUSION

In this work, we demonstrate that the quasiparticle bands extrema are renormalized by the many-body effects in homo-bilayers WSe_2 and $MoTe_2$. Consequently, the energy difference $\Delta^v_{K-\Gamma}$ between the K and Γ valley extrema increases by hundreds of meV due to many-body effects. The VBM is located at the K valley for all stacking configurations. To efficiently capture dielectric screening effects from environments, we have developed a "fractional folding" technique that enables dielectric embedding GW calculations in the TMD unit cell, while taking into account the many-body effects from h-BN substrate or encapsulation. Our results demonstrate that the external screening effects from h-BN can reduce $\Delta^v_{K-\Gamma}$ quantitatively, while the VBM remains at the K valley. Moreover, we compared the moiré potentials obtained from various theoretical approaches. Compared to DFT-calculated moiré potentials, the depths of the moiré potentials are increased by 36-52% when many-body effects are incorporated. The continuum model exhibits a renormalized first moiré mini bandwidth as a function of the twist angle. Based on this model, many-body effects result in a larger "magic angle" compared to DFT results.

Acknowledgment

D.L. was supported by the National Science Foundation (NSF) grant No. DMR-2124934. L.Y. was supported by NSF grant No. DMR-2118779. Z.-F.L. was supported by an NSF CAREER award, DMR-2044552, and an Alfred P. Sloan Research Fellowship (FG-2024-21750). This work used Anvil at Purdue University through allocation DMR100005, and Bridges-2 at Pittsburgh Supercomputing Center through allocation PHY220043, both from the Advanced

Cyberinfrastructure Coordination Ecosystem: Services & Support (ACCESS) program, (79) which is supported by NSF grants #2138259, #2138286, #2138307, #2137603, and #2138296.

*Correspondence author: lyang@physics.wustl.edu, zfliu@wayne.edu,

FIGURES:

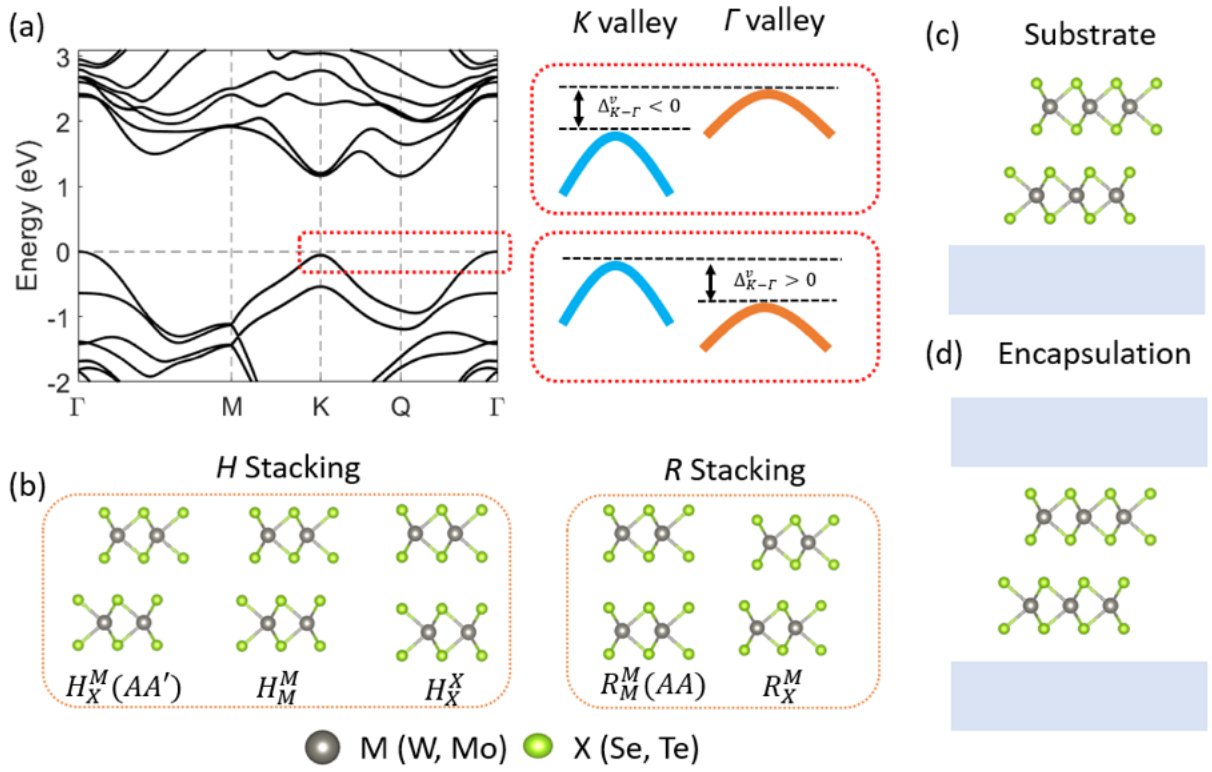

FIG. 1. (a) Typical TMD bilayer electronic band structure. The inset is a schematic illustration of the band extrema offset at the Γ and K valleys. (b) Common local high symmetry stacking configurations in TMD moiré bilayer systems. The two layers exhibit a 180° relative rotational orientation for H stackings. Conversely, the two layers orient in the same direction for R stackings. The superscript and subscript indicate the vertical overlap of X and M atoms, where M represents transition-metal elements and X presents chalcogen elements. There is another R_M^X stacking not shown in the figure, which has a degenerate electronic structure with R_X^M. (c,d) Schematic illustration of external screening environment for (c) substrate and (d) encapsulation, respectively.

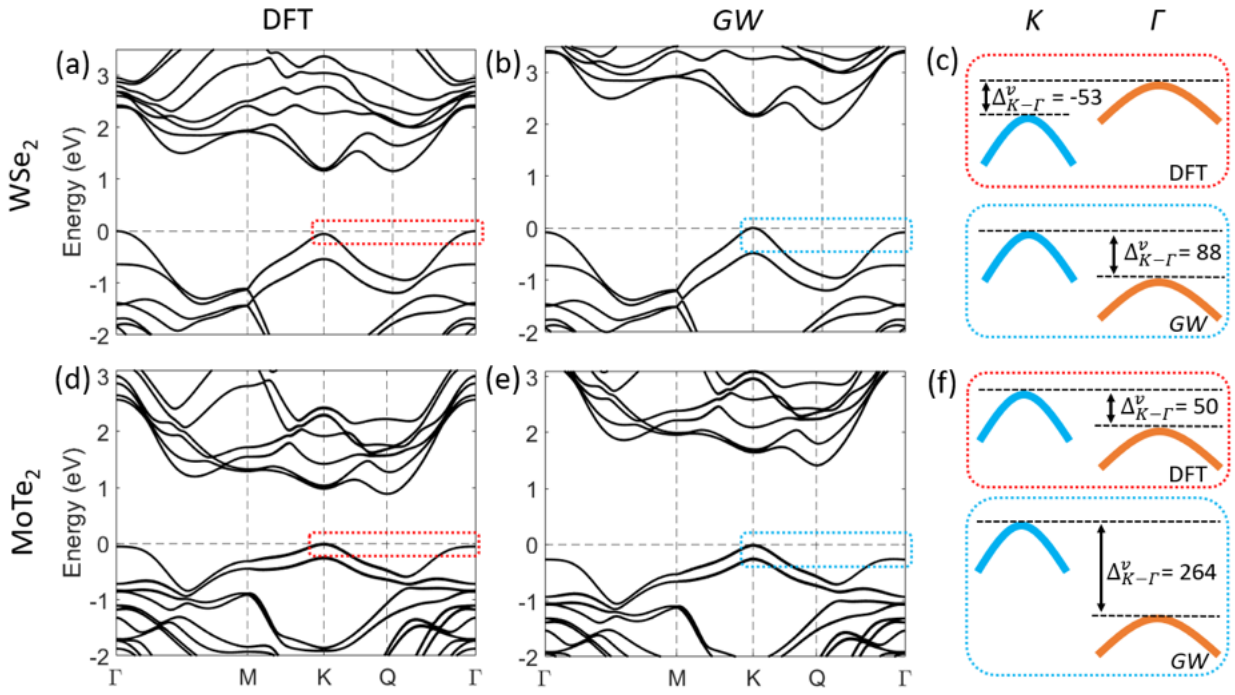

FIG. 2. Bilayer TMD electronic band structure for natural bulk $H_X^M(AA')$ stacking. (a,d) DFT electronic band structure for bilayer (a) WSe_2 and (d) $MoTe_2$. (b,e) Quasiparticle band structure for bilayer (b) WSe_2 and (e) $MoTe_2$. (c,f) Schematic illustration of the band extrema offset at the Γ and K valleys corresponding to the dashed boxes for bilayer (c) WSe_2 and (f) $MoTe_2$. The red and blue dashed boxes represent DFT and GW results, respectively. $\Delta^v_{K-\Gamma} = K_v - \Gamma_v$ (unit: meV) measures the energy difference between the valence band extrema at K and Γ valleys.

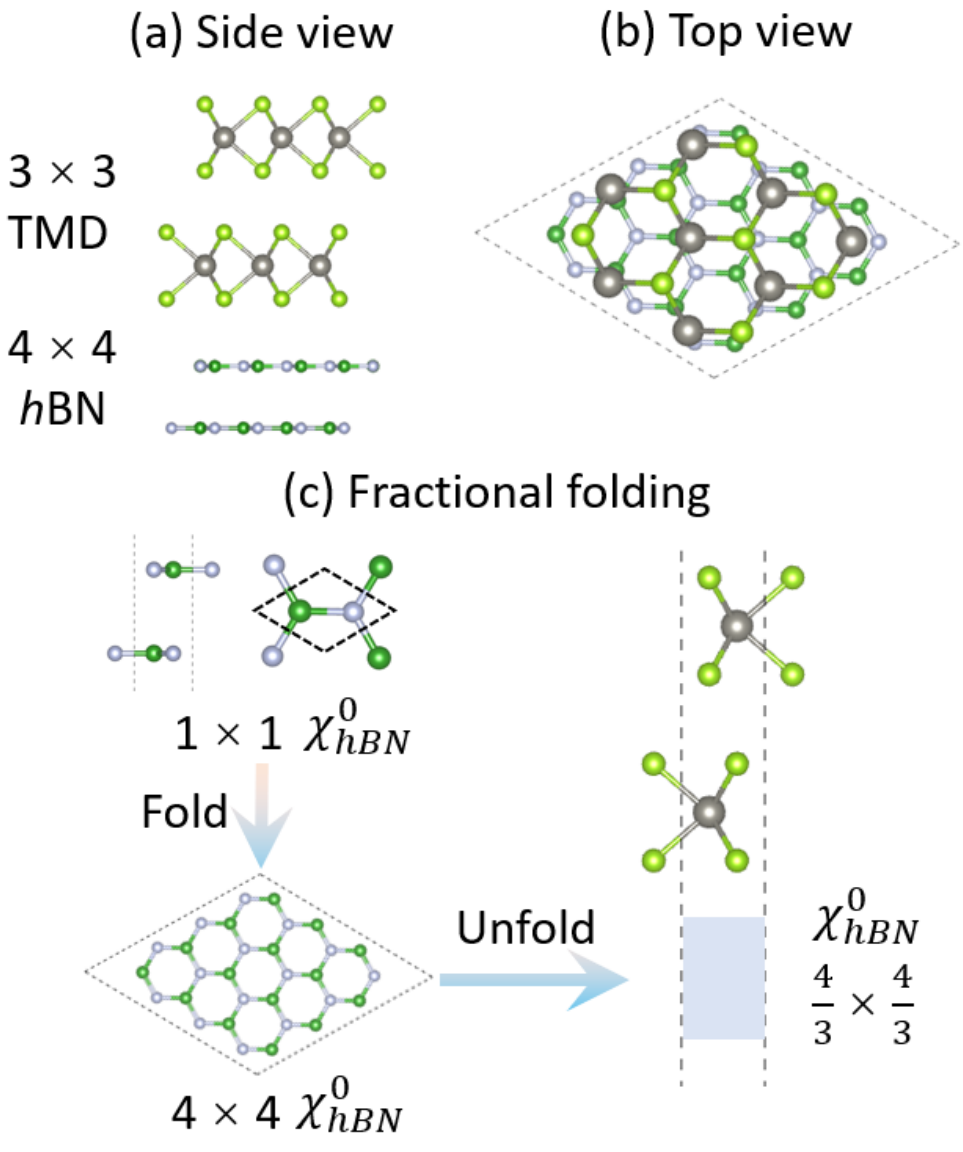
(a) Side view
(b) Top view
3 × 3
TMD
4 × 4
hBN
(c) Fractional folding
1 × 1 χ^0_{hBN}
Fold
4 × 4 χ^0_{hBN}
Unfold
χ^0_{hBN}
$\frac{4}{3} \times \frac{4}{3}$

FIG. 3. (a) a side view and (b) a top view of the TMD/*h*-BN interface supercell. (c) Schematic illustration for including *h*-BN substrate using the "fractional folding" technique.

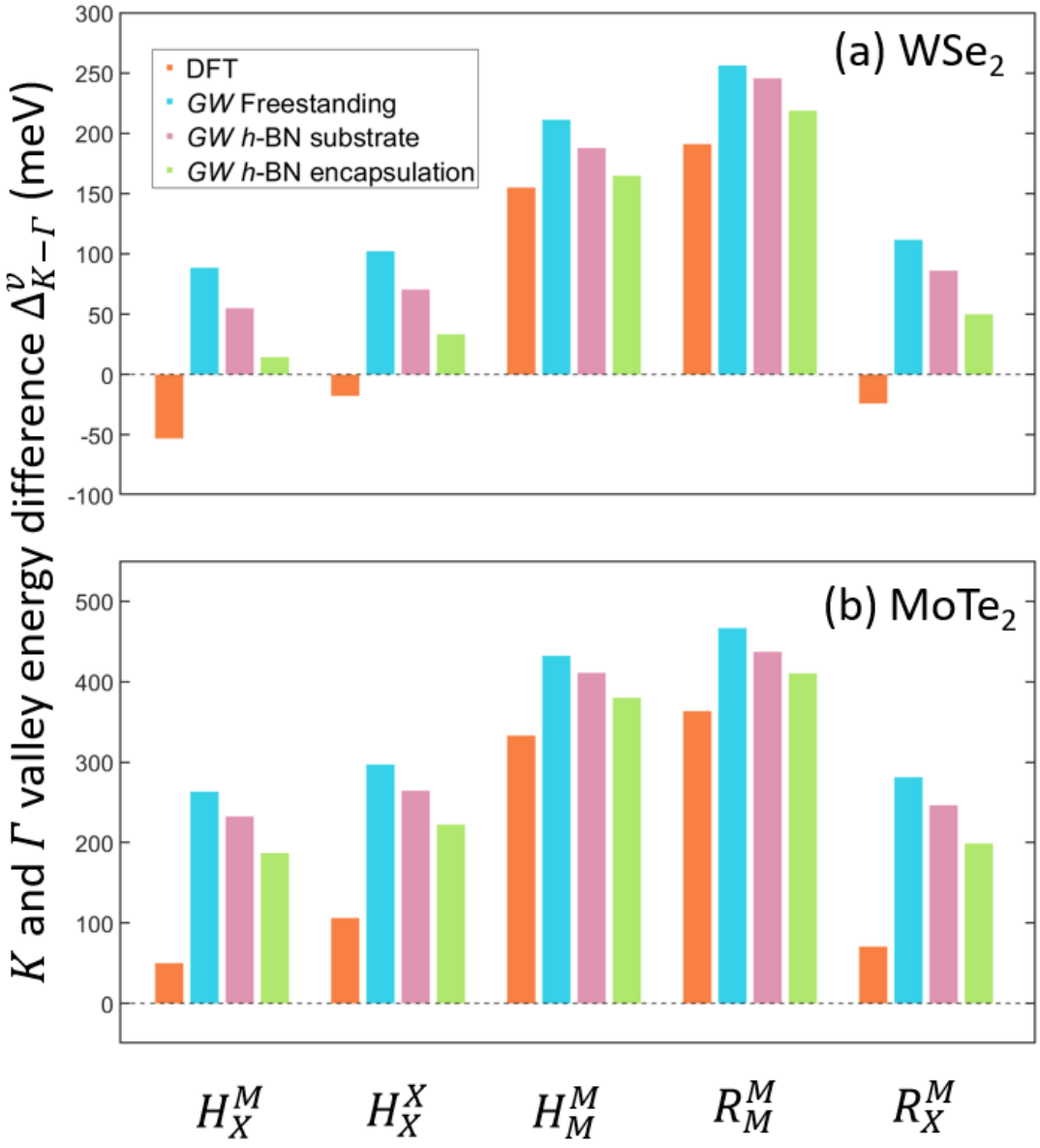

FIG. 4. Energy extrema difference between valence *K* and *Γ* valleys of (a) bilayer WSe_2 and (b) bilayer $MoTe_2$. Different color bars correspond to the different theoretical methods.

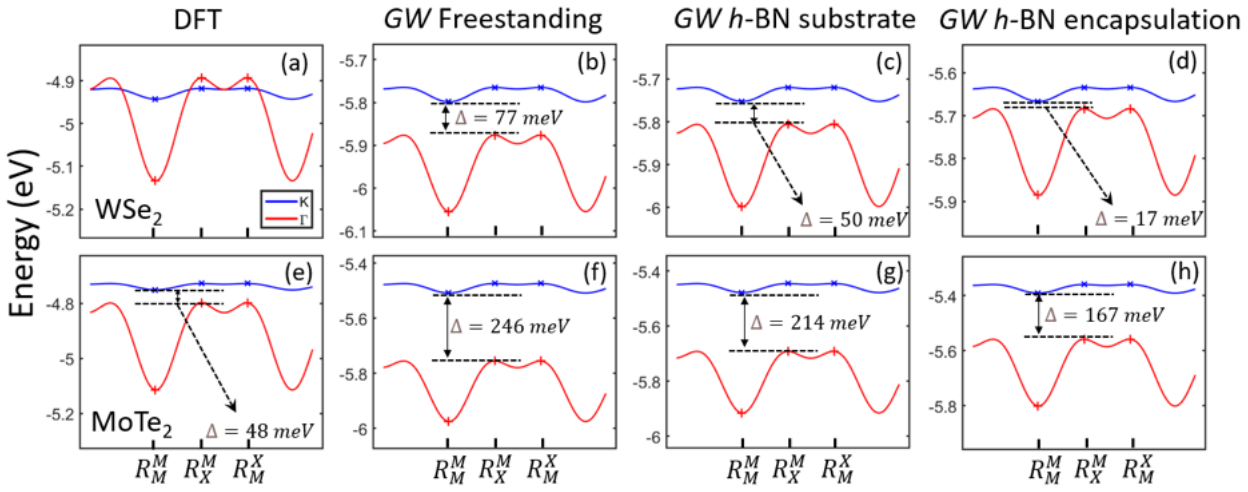

FIG. 5. Moiré potentials obtained by different theoretical methods for WSe_2 (a-d) and $MoTe_2$ (e-h). The red and blue lines are moiré potentials that originate from the valence *Γ* and *K* valleys, respectively. The vacuum level is set to zero.

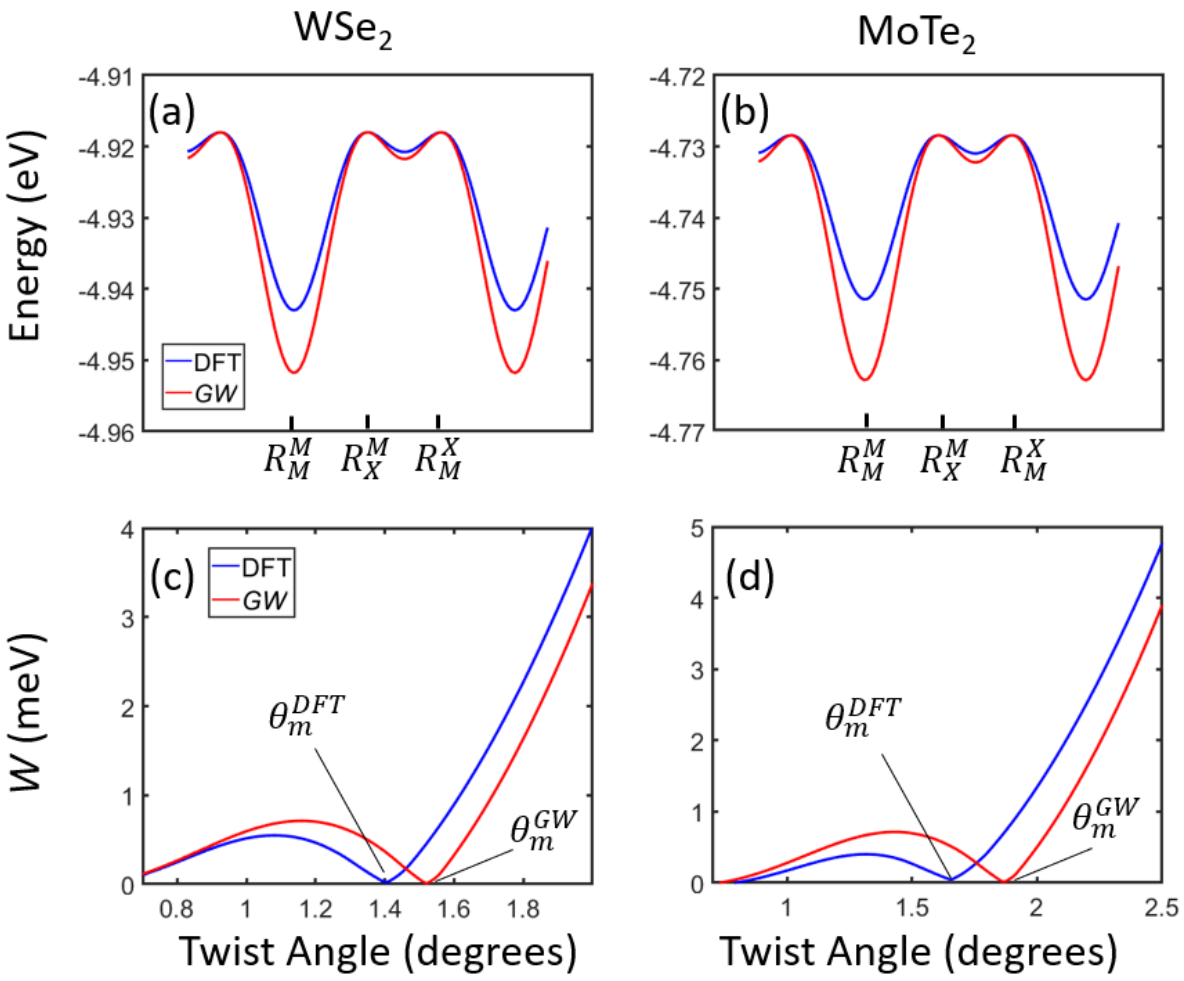

FIG. 6. (a,b) The *K* valley moiré potentials obtained by DFT and *GW* calculations for bilayer (a) WSe_2 and (b) $MoTe_2$. The maxima of the DFT and *GW* curves are aligned to enable an easy comparison of the depth. The DFT potential is measured with respect to the vacuum level. (c,d) The bandwidth of the first moiré band, *W*, versus the twist angle for bilayer (c)

WSe_2 and (d) $MoTe_2$. θ_m^{DFT} and θ_m^{GW} is the magic angle (where $W = 0$) obtained from DFT and *GW* calculations, respectively.

TABLE:

			Gap (eV)		$\Delta^v_{K-\Gamma}$(meV)		Δ^c_{K-Q}(meV)	
	Stacking	d_0 (Å)	DFT	*GW*	DFT	*GW*	DFT	*GW*
WSe_2	$H_X^M(AA')$	6.42	1.219	2.160	**-53**	**88**	8	260
	H_M^M	6.48	1.211	2.158	**-18**	**102**	**-46**	**217**
	H_X^X	7.07	1.217	2.176	155	211	**-50**	**227**
	$R_M^M(AA)$	7.06	1.186	2.150	191	256	16	290
	R_X^M	6.41	1.152	2.097	**-24**	**112**	9	298
$MoTe_2$	$H_X^M(AA')$	7.01	0.980	1.651	50	264	95	240
	H_M^M	7.10	0.969	1.646	106	297	38	189
	H_X^X	7.66	0.994	1.681	333	432	40	172
	$R_M^M(AA)$	7.68	0.961	1.652	364	467	32	148
	R_X^M	7.02	0.933	1.607	71	281	42	179

TABLE I. Electronic band gap and band extremum energy difference for bilayer WSe_2 and $MoTe_2$. d_0 is calculated equilibrium interlayer distance measured as the vertical distance between the W or Mo atoms on the neighbor layers. The K-to-K direct gap is presented. $\Delta^v_{K-\Gamma} = K_v - \Gamma_v$ presents energy difference between the valence band extremum at the K and Γ valleys. $\Delta^c_{K-Q} = K_c - Q_c$ presents energy difference between the conduction band extremum at the K and Q valleys. The bold fonts indicate that many-body effects reverse the sign of $\Delta^v_{K-\Gamma}$ or Δ^c_{K-Q} compared to the DFT results.

REFERENCES

[1] X. Chia, M. Pumera, Layered transition metal dichalcogenide electrochemistry: journey across the periodic table, Chem Soc Rev, 47 (2018) 5602-5613.

[2] A.Y. Eng, A. Ambrosi, Z. Sofer, P. Simek, M. Pumera, Electrochemistry of transition metal dichalcogenides: strong dependence on the metal-to-chalcogen composition and exfoliation method, ACS Nano, 8 (2014) 12185-12198.

[3] R. Roldán, J.A. Silva‐Guillén, M.P. López‐Sancho, F. Guinea, E. Cappelluti, P. Ordejón, Electronic properties of single‐layer and multilayer transition metal dichalcogenides MX2 (M = Mo, W and X = S, Se), Annalen der Physik, 526 (2014) 347-357.

[4] Z. Zhou, J. Lv, C. Tan, L. Yang, Z. Wang, Emerging Frontiers of 2D Transition Metal Dichalcogenides in Photovoltaics Solar Cell, Advanced Functional Materials, 34 (2024) 2316175.

[5] J.R. Schaibley, H. Yu, G. Clark, P. Rivera, J.S. Ross, K.L. Seyler, W. Yao, X. Xu, Valleytronics in 2D materials, Nature Reviews Materials, 1 (2016) 16055.

[6] S.B. Desai, G. Seol, J.S. Kang, H. Fang, C. Battaglia, R. Kapadia, J.W. Ager, J. Guo, A. Javey, Strain-induced indirect to direct bandgap transition in multilayer WSe2, Nano Lett, 14 (2014) 4592-4597.

[7] Z. Wang, Y.H. Chiu, K. Honz, K.F. Mak, J. Shan, Electrical Tuning of Interlayer Exciton Gases in WSe2 Bilayers, Nano Lett, 18 (2018) 137-143.

[8] J. Cai, E. Anderson, C. Wang, X. Zhang, X. Liu, W. Holtzmann, Y. Zhang, F. Fan, T. Taniguchi, K. Watanabe, Y. Ran, T. Cao, L. Fu, D. Xiao, W. Yao, X. Xu, Signatures of fractional quantum anomalous Hall states in twisted MoTe2, Nature, 622 (2023) 63-68.

[9] T. Devakul, V. Crepel, Y. Zhang, L. Fu, Magic in twisted transition metal dichalcogenide bilayers, Nat Commun, 12 (2021) 6730.

[10] W.-X. Qiu, B. Li, X.-J. Luo, F. Wu, Interaction-Driven Topological Phase Diagram of Twisted Bilayer MoTe2, Physical Review X, 13 041026 (2023) 041026.

[11] L. Wang, E.M. Shih, A. Ghiotto, L. Xian, D.A. Rhodes, C. Tan, M. Claassen, D.M. Kennes, Y. Bai, B. Kim, K. Watanabe, T. Taniguchi, X. Zhu, J. Hone, A. Rubio, A.N. Pasupathy, C.R. Dean, Correlated electronic phases in twisted bilayer transition metal dichalcogenides, Nat Mater, 19 (2020) 861-866.

[12] F. Wu, T. Lovorn, E. Tutuc, I. Martin, A.H. MacDonald, Topological Insulators in Twisted Transition Metal Dichalcogenide Homobilayers, Phys Rev Lett, 122 (2019) 086402.

[13] F. Xu, Z. Sun, T. Jia, C. Liu, C. Xu, C. Li, Y. Gu, K. Watanabe, T. Taniguchi, B. Tong, J. Jia, Z. Shi, S. Jiang, Y. Zhang, X. Liu, T. Li, Observation of Integer and Fractional Quantum Anomalous Hall Effects in Twisted Bilayer MoTe2, Physical Review X, 13 031037 (2023) 031037.

[14] K.T.C. Ellis Thompson, F. Mesple, X. -W Zhang, C. Hu, Y. Zhao, H. Park, J. Cai, E. Anderson, K. Watanabe, T. Taniguchi, J. Yang, J. -H Chu, X. Xu, T. Cao, D. Xiao, M. Yankowitz, Visualizing the microscopic origins of topology in twisted molybdenum ditelluride, arXiv:2405.19308.

[15] R. Lv, J.A. Robinson, R.E. Schaak, D. Sun, Y. Sun, T.E. Mallouk, M. Terrones, Transition metal dichalcogenides and beyond: synthesis, properties, and applications of single- and few-layer nanosheets, Acc Chem Res, 48 (2015) 56-64.

[16] S. Bhattacharyya, A.K. Singh, Semiconductor-metal transition in semiconducting bilayer sheets of transition-metal dichalcogenides, Physical Review B, 86 (2012) 075454.

[17] M. Angeli, A.H. MacDonald, Gamma valley transition metal dichalcogenide moire bands, Proc Natl Acad Sci U S A, 118 (2021) e2021826118.

[18] S. Olin, E. Jmukhadze, A.H. MacDonald, W.-C. Lee, Ab initio study of the energy competition between Γ and K valleys in bilayer transition metal dichalcogenides, Physical Review B, 109 (2024) 165101.

[19] P.-C. Yeh, W. Jin, N. Zaki, D. Zhang, J.T. Liou, J.T. Sadowski, A. Al-Mahboob, J.I. Dadap, I.P. Herman, P. Sutter, R.M. Osgood, Layer-dependent electronic structure of an atomically heavy two-dimensional dichalcogenide, Physical Review B, 91 (2015) 041407(R).

[20] G. Gatti, J. Issing, L. Rademaker, F. Margot, T.A. de Jong, S.J. van der Molen, J. Teyssier, T.K. Kim, M.D. Watson, C. Cacho, P. Dudin, J. Avila, K.C. Edwards, P. Paruch, N. Ubrig, I. Gutierrez-Lezama, A.F. Morpurgo, A. Tamai, F. Baumberger, Flat Gamma Moire Bands in Twisted Bilayer WSe2, Phys Rev Lett, 131 (2023) 046401.

[21] Y. Zhang, M.M. Ugeda, C. Jin, S.F. Shi, A.J. Bradley, A. Martin-Recio, H. Ryu, J. Kim, S. Tang, Y. Kim, B. Zhou, C. Hwang, Y. Chen, F. Wang, M.F. Crommie, Z. Hussain, Z.X. Shen, S.K. Mo, Electronic Structure, Surface Doping, and Optical Response in Epitaxial WSe2 Thin Films, Nano Lett, 16 (2016) 2485-2491.

[22] W. Zhao, X. Zhou, D. Yan, Y.a. Huang, C. Li, Q. Gao, H. Rong, Y. Cai, E.F. Schwier, D. Ju, C. Shen, Y. Wang, Y. Xu, W. Ji, Y. Shi, L. Zhao, L. Bao, Q. Wang, K. Shimada, X. Tao, H. Gao, Z.-Y. Xu, X. Zhou, G. Liu, Direct Measurement of the Electronic Structure and band gap nature of atomic-layer-thick 2H-MoTe2, arXiv:2001.05894.

[23] H.-g. Kim, H.J. Choi, Thickness dependence of work function, ionization energy, and electron affinity of Mo and W dichalcogenides from DFT and GW calculations, Physical Review B, 103 (2021) 085404.

[24] M.M. Ugeda, A.J. Bradley, S.F. Shi, F.H. da Jornada, Y. Zhang, D.Y. Qiu, W. Ruan, S.K. Mo, Z. Hussain, Z.X. Shen, F. Wang, S.G. Louie, M.F. Crommie, Giant bandgap renormalization and excitonic effects in a monolayer transition metal dichalcogenide semiconductor, Nat Mater, 13 (2014) 1091-1095.

[25] L. Yang, J. Deslippe, C.H. Park, M.L. Cohen, S.G. Louie, Excitonic effects on the optical response of graphene and bilayer graphene, Phys Rev Lett, 103 (2009) 186802.

[26] M.H. Naik, E.C. Regan, Z. Zhang, Y.H. Chan, Z. Li, D. Wang, Y. Yoon, C.S. Ong, W. Zhao, S. Zhao, M.I.B. Utama, B. Gao, X. Wei, M. Sayyad, K. Yumigeta, K. Watanabe, T. Taniguchi, S. Tongay, F.H. da Jornada, F. Wang, S.G. Louie, Intralayer charge-transfer moire excitons in van der Waals superlattices, Nature, 609 (2022) 52-57.

[27] M.S. Hybertsen, S.G. Louie, Electron correlation in semiconductors and insulators: Band gaps and quasiparticle energies, Phys Rev B Condens Matter, 34 (1986) 5390-5413.

[28] J.P. Perdew, K. Burke, M. Ernzerhof, Generalized Gradient Approximation Made Simple, Phys Rev Lett, 77 (1996) 3865-3868.

[29] D. R. Hamann, Optimized norm-conserving Vanderbilt pseudopotentials, Phys. Rev. B, 88 (2013) 085117.

[30] P. Giannozzi, O. Andreussi, T. Brumme, O. Bunau, M. Buongiorno Nardelli, M. Calandra, R. Car, C. Cavazzoni, D. Ceresoli, M. Cococcioni, N. Colonna, I. Carnimeo, A. Dal Corso, S. de Gironcoli, P. Delugas, R.A. DiStasio, Jr., A. Ferretti, A. Floris, G. Fratesi, G. Fugallo, R. Gebauer, U. Gerstmann, F. Giustino, T. Gorni, J. Jia, M. Kawamura, H.Y. Ko, A. Kokalj, E. Kucukbenli, M. Lazzeri, M. Marsili, N. Marzari, F. Mauri, N.L. Nguyen, H.V. Nguyen, A. Otero-de-la-Roza, L. Paulatto, S. Ponce, D. Rocca, R. Sabatini, B. Santra, M. Schlipf, A.P. Seitsonen, A. Smogunov, I. Timrov, T. Thonhauser, P. Umari, N. Vast, X. Wu, S. Baroni, Advanced capabilities for materials modelling with Quantum ESPRESSO, J Phys Condens Matter, 29 (2017) 465901.

[31] S. Grimme, Semiempirical GGA-type density functional constructed with a long-range dispersion correction, J Comput Chem, 27 (2006) 1787-1799.

[32] J. Deslippe, G. Samsonidze, D.A. Strubbe, M. Jain, M.L. Cohen, S.G. Louie, BerkeleyGW: A massively parallel computer package for the calculation of the quasiparticle and optical properties of materials and nanostructures, Computer Physics Communications, 183 (2012) 1269-1289.

[33] S. Ismail-Beigi, Truncation of periodic image interactions for confined systems, Physical Review B, 73 (2006) 233103.

[34] J. Deslippe, G. Samsonidze, M. Jain, M.L. Cohen, S.G. Louie, Coulomb-hole summations and energies for GW calculations with limited number of empty orbitals: A modified static remainder approach, Physical Review B, 87 (2013) 165124.

[35] D.Y. Qiu, T. Cao, S.G. Louie, Nonanalyticity, Valley Quantum Phases, and Lightlike Exciton Dispersion in Monolayer Transition Metal Dichalcogenides: Theory and First-Principles Calculations, Phys Rev Lett, 115 (2015) 176801.

[36] W.G. Dawson, D.W. Bullett, Electronic structure and crystallography of MoTe2and WTe2, Journal of Physics C: Solid State Physics, 20 (1987) 6159-6174.

[37] D.H. Keum, S. Cho, J.H. Kim, D.-H. Choe, H.-J. Sung, M. Kan, H. Kang, J.-Y. Hwang, S.W. Kim, H. Yang, K.J. Chang, Y.H. Lee, Bandgap opening in few-layered monoclinic MoTe2, Nature Physics, 11 (2015) 482-486.

[38] Z. Li, J. Förste, K. Watanabe, T. Taniguchi, B. Urbaszek, A.S. Baimuratov, I.C. Gerber, A. Högele, I. Bilgin, Stacking-dependent exciton multiplicity in WSe2 bilayers, Physical Review B, 106 (2022) 045411.

[39] I.C. Gerber, X. Marie, Dependence of band structure and exciton properties of encapsulated WSe2 monolayers on the hBN-layer thickness, Physical Review B, 98 (2018) 245126.

[40] C. Robert, R. Picard, D. Lagarde, G. Wang, J.P. Echeverry, F. Cadiz, P. Renucci, A. Högele, T. Amand, X. Marie, I.C. Gerber, B. Urbaszek, Excitonic properties of semiconducting monolayer and bilayer MoTe2, Physical Review B, 94 (2016) 155425.

[41] B. Emrem, J.-O. Joswig, T. Heine, Precise structure and energy of group 6 transition metal dichalcogenide homo- and heterobilayers in high-symmetry configurations, 2D Materials, 11 (2024) 035011.

[42] Z.F. Liu, F.H. da Jornada, S.G. Louie, J.B. Neaton, Accelerating GW-Based Energy Level Alignment Calculations for Molecule-Metal Interfaces Using a Substrate Screening Approach, J Chem Theory Comput, 15 (2019) 4218-4227.

[43] F. Xuan, Y. Chen, S.Y. Quek, Quasiparticle Levels at Large Interface Systems from Many-Body Perturbation Theory: The XAF-GW Method, J Chem Theory Comput, 15 (2019) 3824-3835.

[44] D. Li, Z.F. Liu, L. Yang, Accelerating GW Calculations of Point Defects with the Defect-Patched Screening Approximation, J Chem Theory Comput, 19 (2023) 9435-9444.

[45] O. Adeniran, Z.-F. Liu, Dielectric screening at TMD:hBN interfaces: Monolayer-to-bulk transition, local-field effect, and spatial dependence, Physical Review Materials, 7 (2023) 054001.

[46] D.Y. Qiu, F.H. da Jornada, S.G. Louie, Environmental Screening Effects in 2D Materials: Renormalization of the Bandgap, Electronic Structure, and Optical Spectra of Few-Layer Black Phosphorus, Nano Lett, 17 (2017) 4706-4712.

[47] A.J. Bradley, M.M. Ugeda, F.H. da Jornada, D.Y. Qiu, W. Ruan, Y. Zhang, S. Wickenburg, A. Riss, J. Lu, S.K. Mo, Z. Hussain, Z.X. Shen, S.G. Louie, M.F. Crommie, Probing the role of interlayer coupling and coulomb interactions on electronic structure in few-layer MoSe2 nanostructures, Nano Lett, 15 (2015) 2594-2599.

[48] M. Del Ben, F.H. da Jornada, A. Canning, N. Wichmann, K. Raman, R. Sasanka, C. Yang, S.G. Louie, J. Deslippe, Large-scale GW calculations on pre-exascale HPC systems, Computer Physics Communications, 235 (2019) 187-195.

[49] Z.F. Liu, Dielectric embedding GW for weakly coupled molecule-metal interfaces, J Chem Phys, 152 (2020) 054103.

[50] H. Wang, L. Yang, Topological phase transition from periodic edge states in moiré superlattices, Physical Review B, 107 (2023) 235427.

[51] M.H. Naik and M. Jain, Ultraflatbands and Shear Solitons in Moiré Patterns of Twisted Bilayer Transition Metal Dichalcogenides, Physical Review Letters 121 (2018) 266401.

[52] X.W. Zhang, C. Wang, X. Liu, Y. Fan, T. Cao, D. Xiao, Polarization-driven band topology evolution in twisted MoTe2 and WSe2, Nat Commun, 15 (2024) 4223.